A Comparative Study of DEM Reconstruction Using the Single-Baseline and Multibaseline InSAR Techniques

Shijie Liu, Hongcheng Tang, Yongjiu Feng, Yanling Chen, Zhenkun Lei, Jiafeng Wang, and Xiaohua Tong, *Senior Member, IEEE*

***Abstract*—Interferometric SAR (InSAR) is a practical technique to derive 3-D structure of the earth's surface. This article conducts a comparative study of digital elevation model (DEM) reconstruction using the single-baseline and multibaseline InSAR techniques. To improve the accuracy of the DEM generated from the single-baseline InSAR, we improve the weight definition approach according to the coherence magnitudes for the fusion of single-baseline InSAR DEMs. For multibaseline InSAR, we adopt a method based on the maximum-likelihood estimation (MLE) algorithm, which uses external DEM as a constraint. A TerraSAR-X dataset comprising four SAR images acquired over Barcelona is used for experimental investigation. The accuracies of four types of DEM are comparatively studied, including DEM by single-baseline InSAR, DEM by the fusion of single-baseline InSAR DEMs, DEM by unconstrained multibaseline InSAR, and DEM by constrained multibaseline InSAR. The results show that the proposed weighted fusion of single-baseline InSAR performed slightly better than the constrained multibaseline InSAR method, and both of them performed better than the single-baseline results, demonstrating that multiple observations can effectively improve the accuracy of the reconstructed DEM.**

***Index Terms*—Digital elevation model (DEM), interferometric SAR (InSAR), maximum-likelihood estimation (MLE), multibaseline.**

Manuscript received January 4, 2021; revised May 28, 2021; accepted August 10, 2021. Date of publication August 18, 2021; date of current version September 9, 2021. This work was supported in part by the National Key R&D Program of China under Project 2017YFB0502705, in part by the National Natural Science Foundation of China under Project 41631178 and Project 42071371, in part by Shanghai Natural Science Foundation under Project 17ZR1435700, and in part by the State Key Laboratory of Geo-Information Engineering under Project SKLGIE2018-Z-3-2, and in part by the State Key Laboratory for Disaster Reduction in Civil Engineering under Project SLDRCE19-B-36. *(Corresponding authors: Yongjiu Feng; Xiaohua Tong.)*

Shijie Liu is with the State Key Laboratory for Disaster Reduction in Civil Engineering and College of Surveying and Geo-Informatics, Tongji University, Shanghai 200092, China, and also with the State Key Laboratory of Geo-Information Engineering, Xi'an 710054, China (e-mail: liusjtj@tongji.edu.cn).

Hongcheng Tang is with the F Squares Technology Company, Ltd., Beijing 100089, China (e-mail: 951563682@qq.com).

Yongjiu Feng, Zhenkun Lei, Jiafeng Wang, and Xiaohua Tong are with the State Key Laboratory for Disaster Reduction in Civil Engineering and College of Surveying and Geo-Informatics, Tongji University, Shanghai 200092, China (e-mail: yjfeng@tongji.edu.cn; zhenkun.lei@foxmail.com; wangjf93024@163.com; xhtong@tongji.edu.cn).

Yanling Chen is with the Shanghai Astronomical Observatory, Chinese Academy of Sciences, Shanghai 200030, China (e-mail: ylchen@shao.ac.cn).

Digital Object Identifier 10.1109/JSTARS.2021.3105231

I. Introduction

DIGITAL elevation models (DEMs), as digital expressions of the terrain, have been widely used in surveying, mapping, building design, and disaster reduction [1], [2]. DEMs can be produced using several approaches such as topographic survey, light detection and ranging (LiDAR), and aerial/space photogrammetry [3]. While topographic survey has high accuracy at the survey sites, the accuracy of the DEMs generated by this method is limited by the number of survey points [4]. This method is thus not fully suitable for the mapping of wide areas. LiDAR and aerial photogrammetry techniques largely improve the efficiency of topographic survey, but they are expensive approaches that strongly rely on equipment [3]. Since the 2000s, space-borne photogrammetry has been widely used to generate DEMs due to its high efficiency and low cost. However, optical satellite platforms such as SPOT and ZY-3 cannot acquire the surface information on rainy days or at night, leading to the problem of insufficient data when producing large-scale DEMs [5]–[7]. The emergence of space microwave remote sensing techniques such as synthetic aperture radar (SAR) has addressed the problem of weather limitation [8], [9].

Interferometric SAR (InSAR) is a practical technique to derive three-dimensional information of the earth's surface using either one antenna to repeat orbit measurement or using dual antenna simultaneous measurement for topographical measurement, making use of the phase information of SAR systems for interference processing [10], [11]. Stereo SAR effectively solves the problem of incoherence through images with overlapping areas observed in different directions. This technique reduces the information loss caused by overlap and shadows, and can effectively derive three-dimensional information of the earth's surface [12]. However, stereo SAR has restrictions on the intersection angle of the stereo image when producing the high-precision three-dimensional information of the earth's surface, where the terrain substantially affects the accuracy of stereo positioning [13]. InSAR is currently a more popular approach to produce DEMs. For the InSAR method, the key issue is phase unwrapping (PU) when generating surface elevation.

In the single-baseline InSAR technique, the combination of short baselines can generate sparse fringes and strongly coherent interferograms, facilitating subsequent PU processing. The combination of long baselines theoretically can improve the

accuracy of elevation measurement, but it may result in dense interferogram fringes and low coherence quality, consequently leading to more PU errors and even PU failures [14]. Traditional single-baseline PU methods can be roughly categorized into the following three groups.

1) Path tracking integration methods [15].
2) Minimum norm methods [16].
3) Minimum cost flow methods [17].

However, these single-baseline PU methods may cause PU difficulties due to terrain discontinuity or the SAR image noise [18]. To improve the accuracy of single-baseline InSAR PU, external DEMs are usually used as prior information to assist in the unwrapping process. Luo *et al.* [19] proposed a baseline linear combination approach to generate interferograms with nearly zero baselines, minimizing the effects of the uncertainties in the external DEM. Choi and Kim [20] derived phase errors of interferograms using the relationship between the InSAR coherence and the PDF of the phase deviations, and simulated high accuracy InSAR DEMs to detect topographic changes in tidal flats.

InSAR multichannel systems produce more than one interferogram in a multifrequency or multibaseline configuration, allowing the reconstruction of highly sloped and discontinuous terrain height profiles [21]. Multibaseline InSAR height estimation is known as an effective way to facilitate the PU by increasing the ambiguity intervals and maintaining good height measurement sensitivity, especially in mountainous areas. Common methods of multibaseline PU include the Chinese remainder theorem method [21], linear combination method [22], maximum-likelihood phase estimation method [23]–[25], and maximum *a posteriori* estimation based on a Bayesian framework [26]. Studies show that these methods possess weak robustness of noise reduction due to their mathematical foundations. As such, different multibaseline PU algorithms have been proposed based on the unscented Kalman filter [27] or the extended Kalman filter [28]. In addition, there are a few other methods that are not yet in common use, and these include the dual-baseline PU method from the TanDEM-X data [14], and the dual-baseline PU correction framework for the processing the data of the TanDEM-X mission [29]. We have also noticed some new PU methods, such as phase-gradient jump connection based PU and triangle-oriented space-time PU algorithms [30], [31]. However, most of these methods are very sensitive to SAR image noise. The main reason is that they work on pixels and process the PU of each pixel independently of the surrounding pixels. Therefore, an InSAR denoising method based on convolutional sparse coding is proposed to suppress interferometric phase noise and preserve the details [32]. Dong *et al.* [33] multiplied the PDF of the external DEM related to all pixels with the joint density function constructed by the multibaseline maximum-likelihood algorithm. The method introduced *a priori* information with good quality to suppress the influence of noise and produced a better DEM with higher precision. However, when inputting a low-accuracy external DEM and a high-quality interferogram, this algorithm may weaken the probability corresponding to the true value, causing a relatively lower accuracy of the DEM inversion than the result before the external DEM is applied. To adapt well to complex terrain conditions, Dong *et al.* [34] redefined the prior height probability by taking into consideration the local terrain conditions and neighboring height constraints. This work incorporates local elevation constraints and achieves a high-precision DEM even under complex terrain conditions, such as in mountainous areas.

In this study, we focus on the following two issues: 1) can the elevation accuracy be improved using DEM fusion by considering the coherence magnitudes? and 2) how does the performance of the multibaseline InSAR compare with that of the single-baseline InSAR in terms of DEM reconstruction? To improve the applicability of the DEM reconstruction using the InSAR techniques, we improved the weight definition approach of the DEM fusion for single-baseline InSAR and conducted a comparative study of DEM reconstruction using the single-baseline and multibaseline InSAR techniques.

II. Methodology

A. Workflow

The single-baseline InSAR techniques for DEM reconstruction usually require external DEM constraints to improve the PU accuracy [34]. In this study, we derived DEM from the interferometric processing of the SAR image pair and the coherence map (see Fig. 1). We acquired the optimized weights to reconstruct the DEM according to the coherence map. For multibaseline InSAR, we performed interference processing on each image pair, calculated the PDF of the phase with respect to the ground elevation, and produced the refined ground elevation through maximum-likelihood estimation (MLE). Subsequently, a comparative study of the DEMs from the single-baseline and multibaseline methods was conducted.

B. Single-Baseline InSAR and Weighted DEM Fusion

The InSAR altimetry technique acquires repeated observation data of the same area through simultaneous observation by two pairs of antennas (i.e., cross-track interferometry or along-track interferometry mode) or by two parallel observations (i.e., repeat-track interferometry mode) [35]–[37]. The InSAR technique makes full use of the phase information of the radar echo signal [11]. The SAR image pair for interference can be used to derive the related phase differences, and can be combined with the orbit parameters of the observation platform to generate high-precision and high-resolution ground elevation information [38]. Fig. 2 shows the geometric model of InSAR, where S_1 and S_2 are imaging positions of the two SAR systems in the same area, H is the orbital height of satellite S_1, h is the height of the ground observation point P, θ is the incident angle, r is the slant distance from the position of satellite S_1 to target P, and $r + \delta_r$ is the distance from satellite S_2 to the observation point. The vector between S_1 and S_2 antennas is the spatial baseline L, and α is the angle between baseline L and the horizontal direction.

Each pixel in the InSAR interferometric complex image records the phase of the echo signal between the observation target and the satellite. After calibrating the interferometric

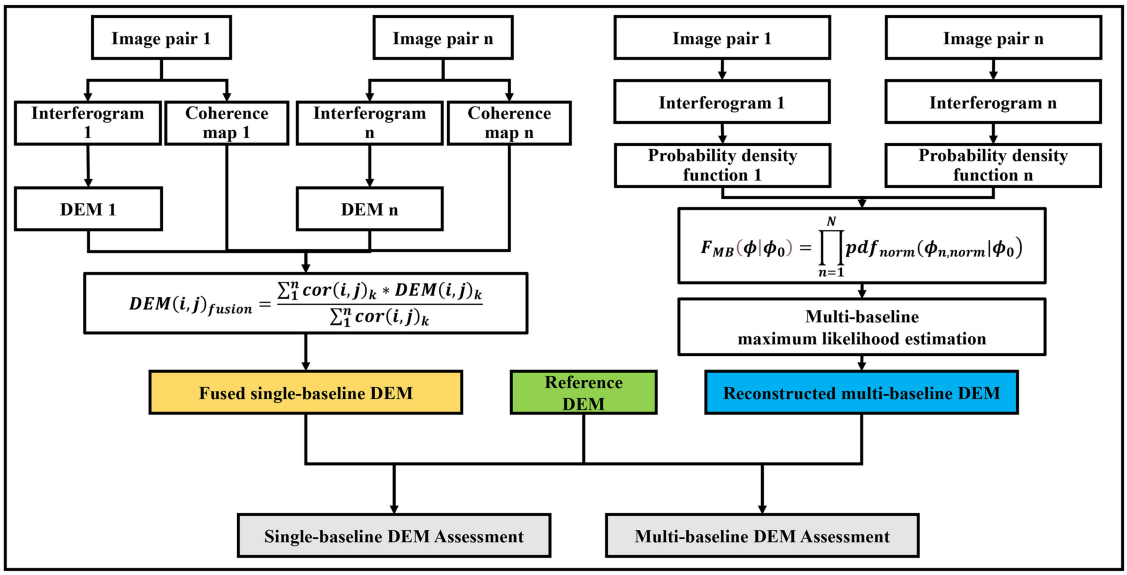

Fig. 1. Workflow of the comparative study of DEM reconstruction using the single-baseline and multibaseline InSAR techniques.

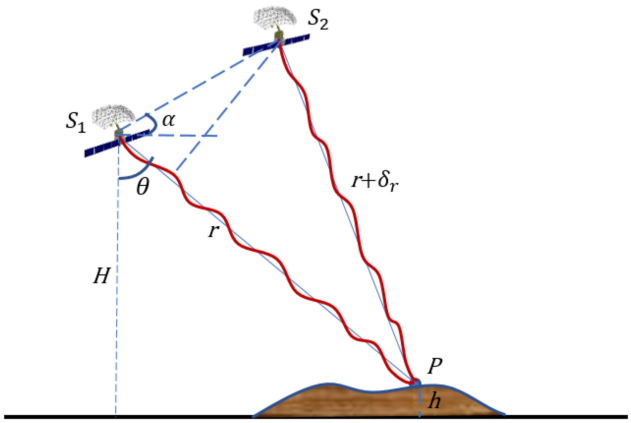

Fig. 2. Schematic diagram of DEM reconstruction using single-baseline InSAR [18].

complex image pair, the recorded phases are different for the same object target due to the difference in the distance between the satellite and the target during the two observations. The phase difference can be given by

$$\Delta\varphi = \varphi_1 - \varphi_2 = -\frac{4\pi}{\lambda} R\,[r-(r+\delta_r)] = \frac{4\pi}{\lambda} R\delta_r \quad (1)$$

where φ_1 and φ_2 are the recorded phases of the echo signal between the observation target and the interferometric complex image pair, respectively; $\Delta\varphi$ is the phase delay of the same observation target in the interferometric complex image pair; and λ is the wavelength of the SAR sensor [39].

The elevation of the ground observation target can be derived from the geometric functions [18]

$$\begin{cases} (r+\delta_r)^2 = r^2 + L^2 - 2rL\cos(\alpha+90^\circ-\theta) \\ h = H - \frac{L^2-{\delta_r}^2}{2[\delta_r+L\sin(\theta-\alpha)]}\cos\theta \end{cases}. \quad (2)$$

To improve the accuracy of the DEM reconstruction of the single-baseline InSAR technique, we fused the multiple single-baseline InSAR DEMs using the weighted average fusion method based on the coherence magnitudes. Since the SAR uses side-view imaging, the information acquired from different angles is different. The elevation is considered reliable when the coherence magnitude is greater than a predefined threshold [40]. The threshold can be determined through experiments using SAR images in the study area and in our experiments the threshold was set as 0.3. The coherence magnitudes of the pixels whose values are smaller than the threshold were set as 0 and the corresponding elevations are considered unreliable. The fused DEM can be given by

$$DEM(i,j)_{\text{fusion}} = \frac{\sum_1^n cor(i,j)_k * DEM(i,j)_k}{\sum_1^n cor(i,j)_k} \quad (3)$$

where cor is the coherence magnitude of the interferometric image pair, DEM is the DEM derived by the single-baseline InSAR technique, DEM_{priori} and DEM_{fusion} are the *a priori* DEM and fused DEM, respectively, (i,j) indicates the pixel position in the image, and n is the number of single-baseline DEMs. It is worth noting that when the coherence magnitudes are all zero, the elevation of the fused DEM inherits from the *a priori* DEM. Compared with the weights determined by accuracy statistics of individual DEMs or correlation statistics, the coherence magnitudes were used as weights that are corresponding to individual pixels in our method, which is more reasonable than using a uniform weight for all the points of a DEM.

C. Multibaseline InSAR for DEM Reconstruction

The multibaseline InSAR produces multiple interferograms and helps to reconstruct the DEM [21]. However, due to the existence of integer ambiguity, the elevation of the ground target can be expressed as the PDF of the phase information [33]. The multibaseline configurations of the InSAR system could lead to different PDFs for the same observation target.

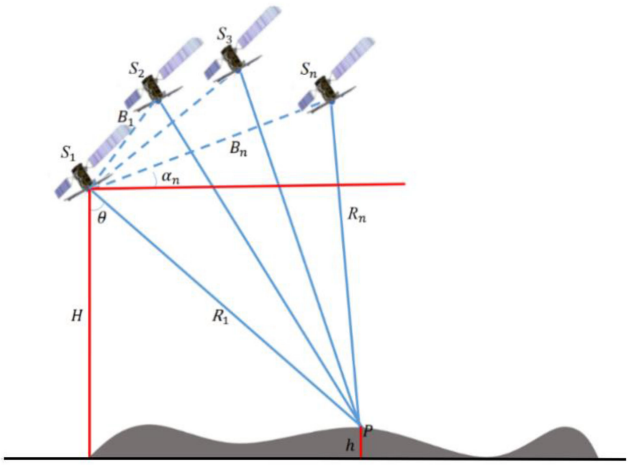

Fig. 3. Schematic diagram of DEM reconstruction using multibaseline InSAR [22].

Fig. 3 shows the geometric principles of the multibaseline InSAR technique, where S_1, S_2, S_3 , and S_n relate to the radar antennas in different positions, *H* and *h* indicate the height of the radar platform and the ground target *P*, respectively, and α_n denotes the angle between the baseline and the horizontal direction. The interference phases are proportional to the baseline length, which can be given as

$$\xi_n = \frac{\phi_n}{\phi_l} = \frac{\frac{2m\pi B_{n\perp}}{\lambda R \sin\theta} h}{\frac{2m\pi B_{l\perp}}{\lambda R \sin\theta} h} = \frac{B_{n\perp}}{B_{l\perp}} \tag{4}$$

where B_n indicates the baseline length of the main antenna S_1 to the antenna S_n and B_l indicates the baseline length of the main antenna S_1 to the antenna S_l. $B_{n\perp}$ and $B_{l\perp}$ are the vertical baseline lengths corresponding to B_n and B_l, respectively, and R is the distance from the radar to the target [41].

By following the multibaseline maximum-likelihood PU method [42], we analyzed the probability distribution of the interference phase of the interferogram. In this method, different interference phases are independent of each other. For the case using a single-baseline, the PDF of the interference phase can be given by

$$\mathrm{PDF}\ (\phi\phi_0) = \frac{1}{2\pi} \frac{1-|\gamma|^2}{1-|\gamma|^2\cos^2(\phi-\phi_0)} \cdot \left[1 + \frac{\zeta \arccos(-\zeta)}{\sqrt{1-\zeta^2}}\right] \tag{5}$$

where $|\gamma|$ denotes the value of the coherence magnitude, ϕ denotes a real interferometric phase, and ϕ_0 denotes the estimate of the real phase. $\zeta = |\gamma|\ \cos(\phi - \phi_0)$. The interval of the PDF is $2\,\pi$ due to the cosine operation of the phase difference. When the difference between the wrapped phase ϕ and the wrapped phase ϕ_0 is integer multiples of 2π , the maximum PDF can be derived. Therefore, phase estimation can be conducted by detecting the maximum PDF, and there may be multiple maximum solutions for a single-baseline [34], [43].

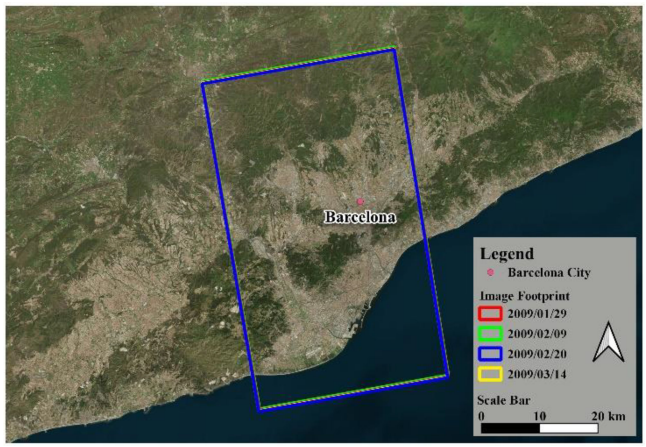

Fig. 4. Study area in Barcelona and the footprints of the SAR images.

The PDF of each pixel in the interferogram can be derived by combining (4) and (5)

$$\mathrm{PDF}_{\mathrm{norm}}\ (\phi_{n,\mathrm{norm}}|\,\phi_0) = \frac{1}{2\pi} \frac{1-|\gamma_n|^2}{1-\omega^2} \cdot \left[1 + \frac{\omega \arccos(-\omega)}{\sqrt{1-\omega^2}}\right] \tag{6}$$

where $\omega = |\gamma_n|\cos(\phi_n - \xi_n\phi_0)$.

The joint PDF and the MLE of phase can be given by

$$\begin{cases} F_{MB}\ (\phi\phi_0) = \prod_{n=1}^{N} \mathrm{PDF}_{\mathrm{norm}}(\phi_{n,\mathrm{norm}}|\phi_0) \\ \phi_{MB}^{l} = arg\max_{\phi_0} F_{MB}\,(\phi\phi_0) \end{cases} \tag{7}$$

where ϕ is the phase set of interferograms, and $\phi_{n,\mathrm{norm}}$ is the *n*th phase of the interferograms [41].

III. Experiments and Discussion

A. Study Area and Datasets

In the experiments, a TerraSAR-X InSAR dataset comprising four SAR images was used for comparative study. Fig. 4 shows the study area and the footprints of the SAR images. TerraSAR-X's optimized system parameters and orbital design allow for a repeat observation period of 11 days, which effectively improves the co-competence of radar interference data [44]. In this study, we used TerraSAR-X SAR images acquired in ascending orbits, which were collected using *X*-band radar in the SM (StripMap) imaging mode. The range sampling spacing and azimuth sampling spacing are 0.91 and 1.89 m, respectively. The SAR images were acquired on January 29, February 9, February 20, and March 14, 2009.

Combinations of the above four SAR images can generate six interference image pairs. Considering the impacts of the spatial baseline and temporal baseline on InSAR to reduce errors caused by low-quality interferograms [18], we selected the image of February 20, 2009 as the master image, and the remaining three images as the slave images of different interference combinations (see Table I).

The SRTM DEM with 90 m spatial resolution [45] was used as a low-resolution external DEM to provide the *a*

TABLE I
BASIC INFORMATION OF THE INSAR IMAGE PAIRS

Image property	InSAR image pair 1	InSAR image pair 2	InSAR image pair 3
Acquisition date (Master)	2009/02/20	2009/02/20	2009/02/20
Acquisition date (Slave)	2009/02/09	2009/01/29	2009/03/14
Temporal baseline	11 days	22 days	22 days
Vertical baseline	150.81 m	86.72 m	-35.61 m
Height ambiguity	-36.73 m	-63.87 m	155.57 m
Mean coherence magnitude	0.55	0.56	0.43

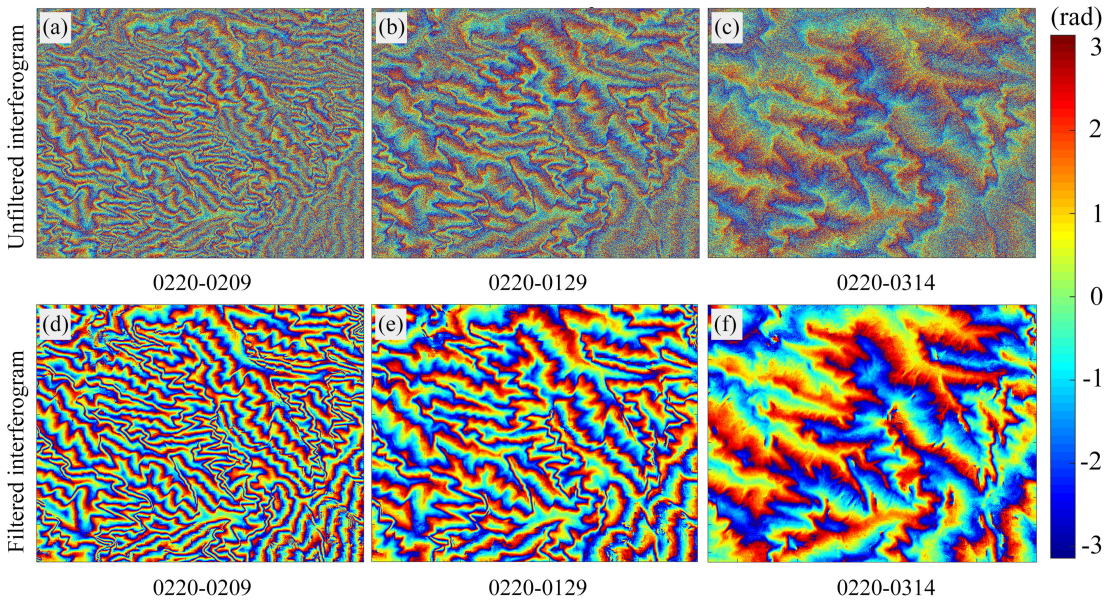

Fig. 5. (a)–(c) Improved Goldstein filter was used to remove the flattened phase in the interferograms and (d)–(f) the improved interferograms.

priori terrain information. The absolute vertical accuracy of the elevation data is approximately 16 m [46].To assess the accuracy of the reconstructed DEMs, we adopted a local DEM with a spatial resolution of 5 m as the reference, which is available from the National Geographic Information Center.[1] This reference DEM is generated by LIDAR data obtained by the photogrammetric and laser scanning missions of the Spanish national plan of aerial ortho-photography.

B. Results of Single-Baseline InSAR and Weighted Fusion

The linearly changing phase produced by the ground surface affects the implementation of PU, and then leads to a low accuracy in InSAR processing [48]. We combined the external DEM and the radar parameters to remove the flattened phase [see Fig. 5(a)–(c)]. Fig. 5(d)–(f) shows that the improved Goldstein filter was used to reduce the phase jump and residuals in the interferograms to improve the PU accuracy [49], [50], and an area with a size of 1872×2200 pixels was selected to show the filter effect and DEM results.

InSAR coherence maps are cross-correlation products derived using two coregistered complex-valued (both the intensity and phase components) SAR images. This eliminates the complicated effects of differently arranged targets on the elementary targets in each pixel. Instead of using the phase to measure the ranges, the difference in phase between two radar images can be used to measure the differences or geometric distortions in ranges between these two images [9]. Thus, the coherence map can be used to evaluate the quality of the interferogram. Fig. 6 shows that the three pairs of interference complex images in the study area have good interference quality.

Among the variety of PU methods, the minimum cost flow method can significantly reduce the time and space complexity of unwrapping and is one of the most promising PU algorithms [17], [51], [52]. The network minimum cost flow method is used for interferogram phase unwrapping, which can convert the phase into a single-baseline DEM by combining it with the radar system parameters. We produced a fused DEM using the single-baseline DEMs and coherence maps. Fig. 7 shows the constructed DEM using the single-baseline InSAR method and the fused DEM.

C. Results of Multibaseline InSAR

We performed two multibaseline DEM reconstruction experiments: 1) unconstrained MLE, which is the unconstrained multibaseline MLE algorithm; and 2) constrained MLE, which

[1][Online]. Available: http://centrodedescargas.cnig.es

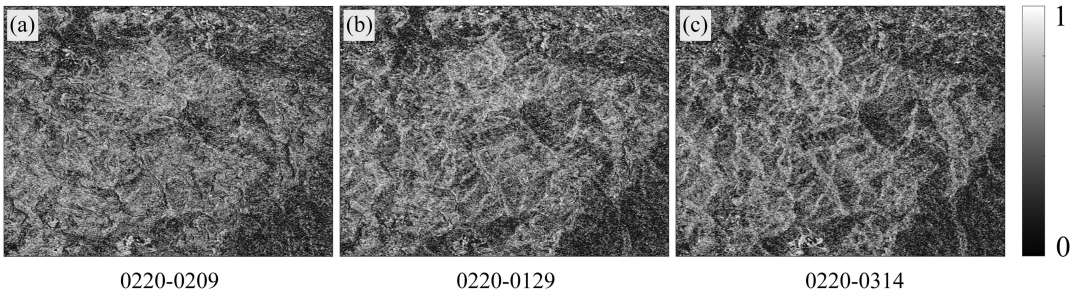

Fig. 6. Coherence maps of the three pairs of interference complex images indicate the good quality of the interferograms.

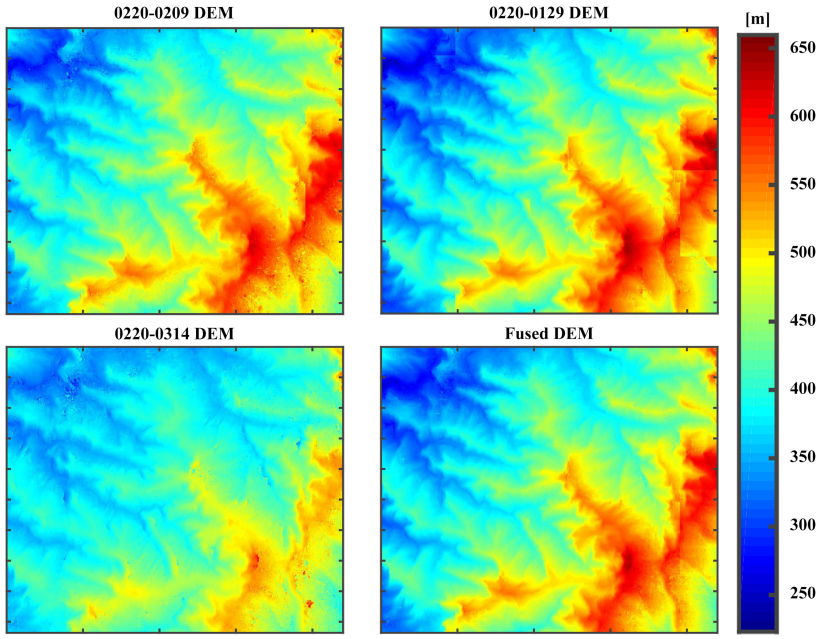

Fig. 7. (a)–(c) Three single-baseline InSAR DEMs. (d) Fused DEM.

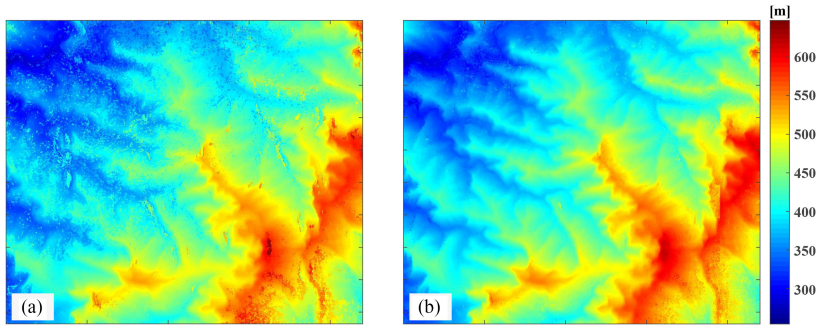

Fig. 8. (a) DEM by the unconstrained MLE multibaseline InSAR. (b) DEM by the constrained MLE multibaseline InSAR.

uses the external DEM as prior information of each pixel to the constrained multibaseline MLE algorithm. Fig. 8 shows the reconstructed multibaseline DEMs using the unconstrained MLE and constrained MLE algorithms. Visual comparison shows that the multibaseline InSAR using the unconstrained MLE was seriously affected by noise in reconstructing the DEM, which displays many burrs. The constrained MLE reduced the influence of the noise by adding elevation constraints, and the generated DEM was continuous with fewer burrs.

D. Comparative Analysis of the InSAR DEM Results

To analyze the accuracy of DEMs derived by the single-baseline InSAR and the fusion techniques, we downsampled the DEMs to the same resolution as the reference DEM and calculated the differences of pixel values as elevation errors. Fig. 9 displays the error distribution of the three single-baseline InSAR DEMs and the fused DEM. Fig. 10 shows the corresponding error histograms. Table II lists the error statistic values.

TABLE II
ELEVATION ERROR OF THE SINGLE-BASELINE INSAR DEMS AND THE FUSED DEM

DEM	Min (m)	Max (m)	Mean (m)	RMSE (m)	Error≤30 m (%)
0220-0209 DEM	-78.2141	87.3157	4.4737	10.8995	98.6989
0220-0129 DEM	-153.5133	90.4793	-0.6140	9.6288	98.2849
0220-0314 DEM	-186.2321	262.3951	-2.8354	20.2674	88.0253
Fused DEM	-54.6879	49.4832	0.5300	7.2323	99.8065

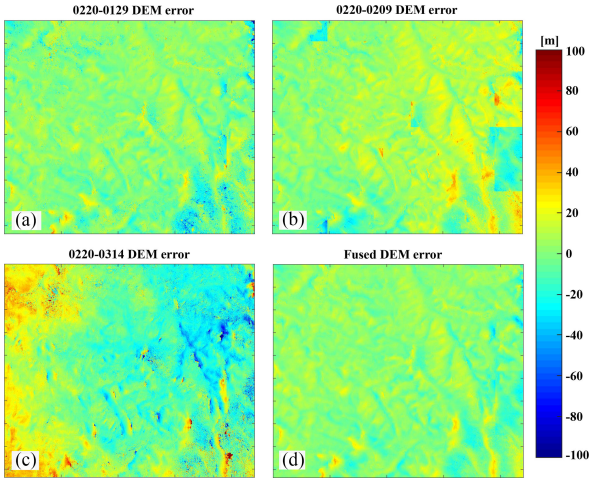

Fig. 9. Elevation errors of (a)–(c) the three single-baseline InSAR DEMs and (d) the fused DEM.

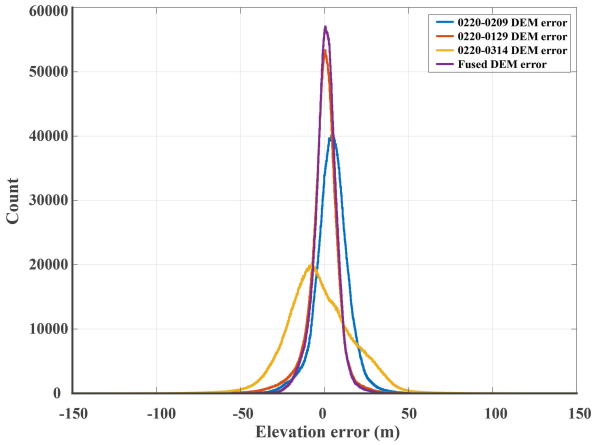

Fig. 10. Histograms of the elevation errors of the single-baseline InSAR DEMs and the fused DEM.

The DEMs were produced by processing two SAR images using the single-baseline InSAR technique, but the accuracy was closely related to the interferometric coherence between the two images. Most areas with large elevation differences were located in places with relatively undulating slopes greater than 5°, indicating that topographic undulation substantially affected the quality of the InSAR DEM. This is because areas with large topographic undulations are often substantially affected by the geometric distortion of SAR images. The image pairs with smaller height ambiguity and higher coherence magnitude have more accurate 3-D information of the earth's surface. The image pair 0220-0209 has the minimum height ambiguity and

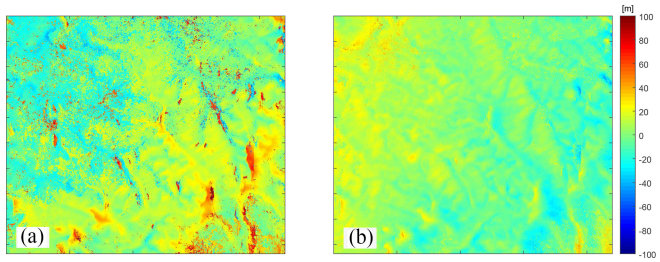

Fig. 11. Elevation errors of (a) the unconstrained MLE multibaseline InSAR DEM and (b) the constrained MLE multibaseline InSAR DEM.

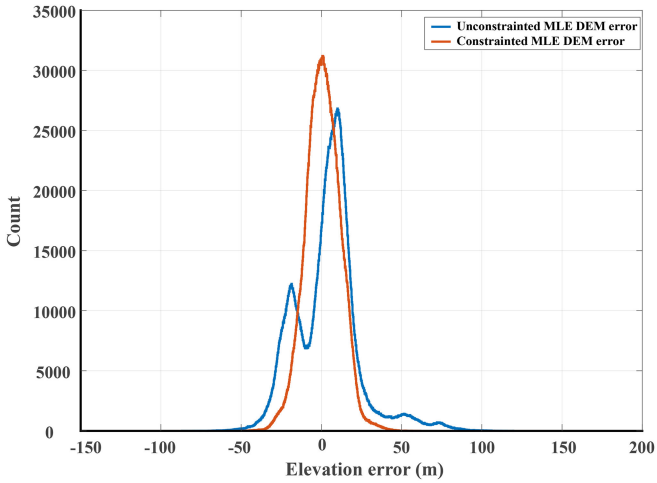

Fig. 12. Histogram of elevation errors of the unconstrained and constrained MLE multibaseline InSAR DEMs.

the image pair 0220-0129 has the maximum mean coherence magnitude (see Table I). The 0220-0129 DEM is more consistent with the reference DEM than other single-baseline InSAR DEMs, indicating that the coherence magnitude has a great influence on the quality of the DEM reconstruction. Using the coherence magnitude as the weight can effectively improve the consistency between the fused DEM and the reference DEM.

Fig. 11 displays the error distribution of the unconstrained and constrained MLE multibaseline InSAR DEMs. Fig. 12 shows the corresponding error histograms. Table III lists the error statistic values. Table III indicates that the errors of the unconstrained MLE DEM are larger than those of the constrained MLE DEM, and the percentage of error less than 30 m of the constrained MLE DEM is higher than that of the unconstrained MLE DEM, indicating that the constrained MLE successfully reduced the influence of noise by adding elevation constraints.

To further compare the accuracies of the DEMs generated by the single-baseline and multibaseline InSAR methods, Fig. 13

TABLE III
ELEVATION ERROR OF THE UNCONSTRAINED AND CONSTRAINED MLE MULTIBASELINE INSAR DEMS

DEM	Min (m)	Max (m)	Mean(m)	RMSE(m)	Error≤30 m (%)
Unconstrained MLE DEM	-86.6439	119.5100	3.7829	20.2614	90.6534
Constrained MLE DEM	-58.7612	61.3842	0.6857	10.9235	98.9493

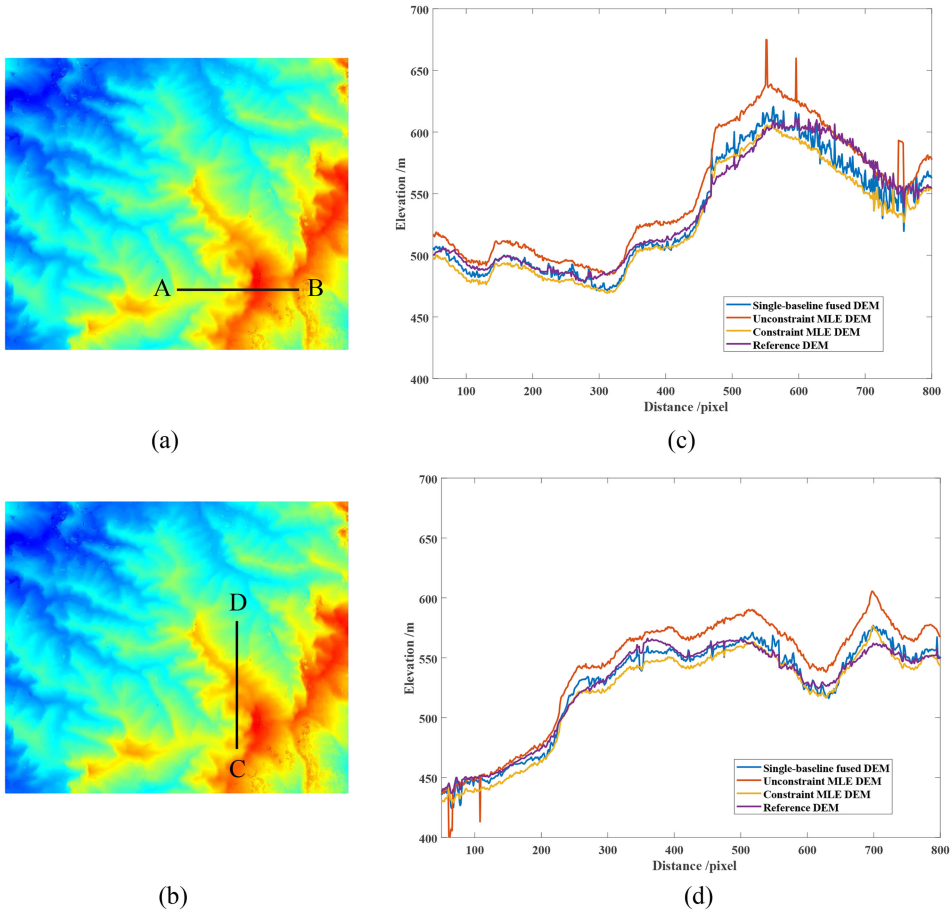

Fig. 13. Elevation profiles derived from the multibaseline InSAR DEM, the single-baseline fused InSAR DEM, and the reference DEM. (a) Profile A-B. (b) Profile C-D. (c) Elevation comparison along A-B profile line. (d) Elevation comparison along C-D profile line.

shows the comparative analysis of the DEMs along the vertical and horizontal profiles. The profiles show that basically the single-baseline fused DEM and the multibaseline DEMs are consistent with the reference DEM, whereas the unconstrained multibaseline DEM is of relatively poor quality. However, the elevation error statistics in Tables II and III show that the single-baseline fused DEM is more consistent with the reference DEM than the constrained MLE multibaseline DEM. Fig. 13(c) and (d) shows that the single-baseline fused DEM has more burrs than the constrained MLE multibaseline DEM, which indicates that the constrained multibaseline method can reduce the influence of the noise with elevation constraints, and the reconstructed DEM is smoother. The geometric distortion caused by the shadow or overlap of the SAR images may lead to incoherence for the single-baseline InSAR, degrading the accuracy of the DEM reconstruction. However, the multibaseline InSAR, which combines multiple sets of interference, can largely avoid the adverse effects caused by the geometric deformation of SAR images and is more robust.

IV. CONCLUSION

This study conducted a comparative study of the single-baseline and multibaseline InSAR DEM reconstruction methods using four scenes of TerraSAR-X SAR images in Barcelona, Spain. For the single-baseline InSAR, three sets of interferograms with different combinations of spatiotemporal baselines were analyzed. In the case of low height ambiguity and large coherence magnitude, the reconstructed DEM has high accuracy. A weight definition approach according to the coherence magnitudes was proposed for the fusion of the single-baseline InSAR DEMs to improve the DEM accuracy. For multibaseline InSAR, unconstrained and constrained MLE algorithms were experimentally investigated. The results showed that the proposed

weighted fusion of single-baseline InSAR performed slightly better than the constrained multibaseline InSAR method, and both of them performed better than the single-baseline results, demonstrating that multiple observations can effectively improve the accuracy of the reconstructed DEM. In our experiments, only the ascending SAR images were used for DEM reconstruction due to the data availability, and both ascending and descending passes will be considered in our future work.

REFERENCES

[1] K. Osborn *et al.*, "National digital elevation program (NDEP)," in *Digital Elevation Model Technologies and Applications: The DEM Users Manual*, 1st ed. Bethesda, MD, USA: Asprs Publications, 2001.

[2] D. Maune, *Digital Elevation Model Technologies and Applications: The DEM Users Manual*, 2nd ed. Bethesda, MD, USA: Asprs Publications, 2007.

[3] A. Belmonte, M. Biong, and E. Macatulad, "DEM generation from close-range photogrammerty using extended python photogrammerty toolbox," presented at the Int. Arch. Photogramm. Remote Sens. Spatial Inf. Sci., Kuala Lumpur, Malaysia, 2017.

[4] A. Patikova, "Digital photogrammetry in the practice of open pit mining," presented at the ISPRS XXth Congress, Istanbul, Turkey, 2004.

[5] M. Tsakiri, G. Olga, and P. Patias, "DEM evaluation generated from HRS SPOT5 data," presented at the ISPRS XXth Congress, Istanbul, Turkey, 2004.

[6] P. Reinartz, R. Müller, D. Hoja, M. Lehner, and M. Schroeder, "Comparison and fusion of DEM derived from SPOT-5 HRS and SRTM data and estimation of forest heights," presented at the Earsel Workshop 3D-Remote Sens., Porto, Portugal, 2005. [Online]. Available: https://elib.dlr.de/19122/

[7] Z. Yanan, D. Fuguang, and Z. Changqing, "DEM extraction and accuracy assessment based on ZY-3 stereo images," presented at the 2nd Int. Conf. Comput. Sci. Netw. Technol., Changchun, China, Dec. 2012.

[8] D. A. Ausherman, A. Kozma, J. L. Walker, H. M. Jones, and E. C. Poggio, "Developments in radar imaging," *IEEE Trans. Aerosp. Electron. Syst.*, vol. AES-20, no. 4, pp. 363–400, Jul. 1984.

[9] Z. Lu and D. Dzurisin, Eds., "InSAR imaging of Aleutian volcanoes," in *InSAR Imaging of Aleutian Volcanoes: Monitoring a Volcanic Arc from Space*. Berlin, Germany: Springer, 2014.

[10] Z. Yang, Q. Zhang, X. Ding, and W. Chen, "Analysis of the quality of daily DEM generation with geosynchronous InSAR," *Engineering*, vol. 6, pp. 913–918, 2020.

[11] M. Honikel, "Improvement of InSAR DEM accuracy using data and sensor fusion," presented at the Sens. Manag. Environ., Seattle, WA, USA, 1998.

[12] K. Eldhuset, "Combination of stereo SAR and InSAR for DEM generation using TanDEM-X spotlight data," *Int. J. Remote Sens.*, vol. 38, no. 15, pp. 4362–4378, 2017.

[13] J. A. Ostrowski and P. Cheng, "DEM extraction from stereo SAR satellite imagery," presented at the IEEE Int. Geosci. Remote Sens. Symp., Honolulu, HI, USA, 2000.

[14] M. Lachaise, T. Fritz, U. Balss, R. Bamler, and E. Michael, "Phase unwrapping correction with dual-baseline data for the TanDEM-X mission," in *Proc. IEEE Int. Geosci. Remote Sens. Symp.*, 2012, pp. 5566–5569.

[15] D. Ghiglia and M. Pritt, *Two-Dimensional Phase Unwrapping: Theory, Algorithms, and Software*. Hoboken, NJ, USA: Wiley, 1998.

[16] R. Cusack, J. Huntley, and H. Goldrein, "Improved noise-immune phase-unwrapping algorithm," *Appl. Opt.*, vol. 34, no. 5, pp. 781–789, 1995.

[17] M. Costantini, "A novel phase unwrapping method based on network programming," *IEEE Trans. Geosci. Remote Sens.*, vol. 36, no. 3, pp. 813–821, May 1998.

[18] P. A. Rosen *et al.*, "Synthetic aperture radar interferometry," *Proc. IEEE*, vol. 88, no. 3, pp. 333–382, Mar. 2000.

[19] H. Luo, Z. Li, Z. Dong, P. Liu, C. Wang, and J. Song, "A new baseline linear combination algorithm for generating urban digital elevation models with multitemporal InSAR observations," *IEEE Trans. Geosci. Remote Sens.*, vol. 58, no. 2, pp. 1120–1133, Feb. 2020.

[20] C. Choi and D. Kim, "Optimum baseline of a single-pass in-SAR system to generate the best DEM in tidal flats," *IEEE J. Sel. Topics Appl. Earth Observ. Remote Sens.*, vol. 11, no. 3, pp. 919–929, Mar. 2018.

[21] Z. Yuan, Y. Deng, F. Li, R. Wang, G. Liu, and X. Han, "Multichannel InSAR DEM reconstruction through improved closed-form robust Chinese remainder theorem," *IEEE Geosci. Remote Sens. Lett.*, vol. 10, no. 6, pp. 1314–1318, Nov. 2013.

[22] W. Xu, E.-C. Chang, L. Kwoh, H. Lim, W. Cheng, and A. Heng, "Phase-unwrapping of SAR interferogram with multi-frequency or multi-baseline," presented at the Geosci. Remote Sens. Symp., Pasadena, CA, USA, Sep. 1994.

[23] M. Eineder and N. Adam, "A maximum-likelihood estimator to simultaneously unwrap, geocode, and fuse SAR interferograms from different viewing geometries into one digital elevation model," *IEEE Trans. Geosci. Remote Sens.*, vol. 43, no. 1, pp. 24–36, Jan. 2005.

[24] M. Schmitt, J. Schönberger, and U. Stilla, "Benefit of using multiple baselines and multiple aspects for SAR interferometry of urban areas," *IEEE J. Sel. Topics Appl. Earth Observ. Remote Sens.*, vol. 7, no. 10, pp. 4107–4118, Oct. 2014.

[25] M. Schmitt and U. Stilla, "Maximum-likelihood estimation for multi-aspect multi-baseline SAR interferometry of urban areas," *ISPRS J. Photogramm. Remote Sens.*, vol. 87, pp. 68–77, 2014.

[26] G. Ferraiuolo, V. Pascazio, and G. Schirinzi, "Maximum a posteriori estimation of height profiles in InSAR imaging," *IEEE Geosci. Remote Sens. Lett.*, vol. 1, no. 2, pp. 66–70, Apr. 2004.

[27] X. Xie and Y. Pi, "Multi-baseline phase unwrapping algorithm based on the unscented Kalman filter," *IET Radar, Sonar Navig.*, vol. 5, no. 3, pp. 296–304, 2011.

[28] B. Osmanoğlu, T. H. Dixon, and S. Wdowinski, "Three-dimensional phase unwrapping for satellite radar interferometry, Part I: DEM generation," *IEEE Trans. Geosci. Remote Sens.*, vol. 52, no. 2, pp. 1059–1075, Feb. 2014.

[29] M. Lachaise, T. Fritz, and R. Bamler, "The dual-baseline phase unwrapping correction framework for the TanDEM-X mission part 1: Theoretical description and algorithms," *IEEE Trans. Geosci. Remote Sens.*, vol. 56, no. 2, pp. 780–798, Feb. 2018.

[30] R. Li, X. Lv, J. Yuan, and J. Yao, "A triangle-oriented spatial–temporal phase unwrapping algorithm based on irrotational constraints for time-series InSAR," *IEEE Trans. Geosci. Remote Sens.*, vol. 57, no. 12, pp. 10263–10275, Dec. 2019.

[31] T. Zhang, X. Lv, J. Qian, J. Hong, and Y. Yun, "Phase unwrapping based on the phase-gradient-jump connections," *Electron. Lett.*, vol. 53, no. 10, pp. 683–685, 2017.

[32] J. Kang, D. Hong, J. Liu, G. Baier, N. Yokoya, and B. Demir, "Learning convolutional sparse coding on complex domain for interferometric phase restoration," *IEEE Trans. Neural Netw. Learn. Syst.*, vol. 32, no. 2, pp. 826–840, Feb. 2021.

[33] Y. Dong, H. Jiang, L. Zhang, M. Liao, and X. Shi, "Improved topographic mapping through multi-baseline SAR interferometry with MAP estimation," presented at the Proc. Fringe Workshop, Frascati, Italy, 2015.

[34] Y. Dong, H. Jiang, L. Zhang, and M. Liao, "An efficient maximum likelihood estimation approach of multi-baseline SAR interferometry for refined topographic mapping in mountainous areas," *Remote Sens.*, vol. 10, no. 3, pp. 454–473, 2018.

[35] U. Wegmüller, A. Wiesmann, T. Strozzi, and M. Santoro, "Initial assessment of the applicability of TerraSAR-X for repeat-track interferometry," presented at the IEEE Int. Geosci. Remote Sens. Symp., Boston, MA, USA, 2008.

[36] R. Bellec, M. Legris, A. Khenchaf, M. Amate, and A. Hetet, "Repeat-track SAS interferometry: Feasibility study," presented at the Proc. OCEANS MTS/IEEE, Washington, DC, USA, 2005.

[37] V. Pascazio, G. Schirinzi, and A. Farina, "Moving target detection by along-track interferometry," presented at the IEEE Int. Geosci. Remote Sens. Symp., Sydney, NSW, Australia, 2001.

[38] Z. Zhao, "Methods on high-accuracy DEM extraction from interferometric SAR in sophisticated terrain areas," *Acta Geodaetica et Cartographica Sin.*, vol. 45, no. 11, pp. 1385–1385, Nov. 2016.

[39] V. B. H. Ketelaar, *Satellite Radar Interferometry: Subsidence Monitoring Techniques (Remote Sensing and Digital Image Processing)*. Berlin, Germany: Springer, 2009, pp. 94–272.

[40] D. Small, F. Holecz, and D. Nuesch, "Combination of ascending/descending ERS-1 InSAR data for calibration and validation," in *Proc. Int. Geosci. Remote Sens. Symp.*, 1995, pp. 553–555.

[41] H. Xu, S. Li, Y. You, A. Liu, and W. Liu, "Unwrapped phase estimation via normalized probability density function for multibaseline InSAR," *IEEE Access*, vol. 7, pp. 4979–4988, 2018.

[42] V. Pascazio and G. Schirinzi, "Estimation of terrain elevation by multifrequency interferometric wide band SAR data," *IEEE Signal Process. Lett.*, vol. 8, no. 1, pp. 7–9, Jan. 2001.
[43] H. Jiang, L. Zhang, Y. Wang, and M. Liao, "Fusion of high-resolution DEMs derived from COSMO-SkyMed and TerraSAR-X InSAR datasets," *J. Geodesy*, vol. 88, pp. 587–599, 2014.
[44] R. Werninghaus and S. Buckreuss, "The TerraSAR-X mission and system design," *IEEE Trans. Geosci. Remote Sens.*, vol. 48, no. 2, pp. 606–614, Feb. 2010.
[45] W. Wu, S. Zhang, and S. Zhao, "Analysis and comparison of SRTM1 DEM and ASTER GDEM V2 data," *J. Geo-Inf. Sci.*, vol. 19, no. 8, pp. 1108–1115, 2017.
[46] EROS, "Shuttle Radar Topography Mission (SRTM) - Mission summary," 2018. [Online]. Available: www.usgs.gov/centers/eros/science/usgs-eros-archive-digital-elevation-srtm-mission-summary
[47] NASA and METI, "ASTER global digital elevation model (GDEM)," 2009. [Online]. Available: https://ssl.jspacesystems.or.jp/ersdac/GDEM/E/4.html
[48] D. Geudtner and M. Schwaebisch, "An algorithm for precise reconstruction of InSAR imaging geometry: Application to 'Flat-Earth' phase removal, phase-to-height conversion and geocoding of InSAR-derived DEMs," presented at the Eur. Conf. Synthetic Aperture Radar, Königswinter, Germany, 1996. [Online]. Available: https://elib.dlr.de/23829/
[49] C. Zhao, Q. Zhang, X. Ding, and J. Zhang, "An iterative Goldstein SAR interferogram filter," *Int. J. Remote Sens.*, vol. 33, no. 11, pp. 3443–3455, 2012.
[50] M. Deng *et al.*, "Improvement and assessment of the absolute positioning accuracy of Chinese high-resolution SAR satellites," *Remote Sens.*, vol. 11, no. 12, pp. 1465–1484, 2019.
[51] M. Lachaise and R. Bamler, "Minimum cost flow phase unwrapping supported by multibaseline unwrapped gradient," presented at the 8th Eur. Conf. Synthetic Aperture Radar, Aachen, Germany, 2010. [Online]. Available: www.researchgate.net/publication/224233769_Minimum_Cost_Flow_phase_unwrapping_supported_by_multibaseline_unwrapped_gradient
[52] X. Tong *et al.*, "Multi-track extraction of two-dimensional surface velocity by the combined use of differential and multiple-aperture InSAR in the Amery Ice Shelf, East Antarctica," *Remote Sens. Environ.*, vol. 204, pp. 122–137, Jan. 2018.

Shijie Liu received the Ph.D. degree in cartography and geographic information engineering from Tongji University, Shanghai, China, in 2012.

He is currently an Associate Professor with the College of Surveying and Geo-Informatics, Tongji University. His research interests include geometric exploitation of high-resolution remote sensing and its applications.

Hongcheng Tang received the M.S. degree in surveying and mapping science and technology from Tongji University, Shanghai, China, in 2020.

He is currently with the F Squares Technology Co., Ltd., Beijing, China.

Yongjiu Feng received the Ph.D. degree in geomatics from Tongji University, Shanghai, China, in 2009.

He is currently a Professor and Associate Dean of the College of Surveying and Geo-Informatics, Tongji University. His research interests include spatial modeling, synthetic aperture radar interferometry, and radar detection of the moon and deep space.

Yanling Chen received the Ph.D. degree in astro-geodynamics from Shanghai Astronomical Observatory, Chinese Academy of Sciences (CAS), Shanghai, China, in 2007.

She is currently a Professor with the Shanghai Astronomical Observatory, CAS. Her research interests include SAR/InSAR theory and applications on land surface deformation monitoring and sea surface wind retrieval, and GNSS/GNSS-R data processing and its remote sensing applications.

Zhenkun Lei received the M.S. degree in marine sciences from Shanghai Ocean University, Shanghai, China, in 2021. He is currently working toward the Ph.D. degree in surveying and mapping science and technology with Tongji University, Shanghai, China.

Jiafeng Wang received the M.S. degree in marine sciences from Shanghai Ocean University, Shanghai, China, in 2020. He is currently working toward the Ph.D. degree in surveying and mapping science and technology with Tongji University, Shanghai, China.

Xiaohua Tong (Senior Member, IEEE) received the Ph.D degree in traffic engineering from Tongji University, Shanghai, China, in 1999.

He is currently a Professor with the College of Surveying and Geo-Informatics, Tongji University. His research interests include photogrammetry and remote sensing, trust in spatial data, and image processing for high-resolution satellite images.